Journal of Catalysis **190,** 261–275 (2000)
doi:10.1006/jcat.1999.2734, available online at http://www.idealibrary.com on

Structural Requirements and Reaction Pathways in Condensation Reactions of Alcohols on Mg_yAlO_x Catalysts

J. I. Di Cosimo,* C. R. Apesteguía,* M. J. L. Ginés,† and E. Iglesia†

**Instituto de Investigaciones en Catálisis y Petroquímica (INCAPE), Santiago del Estero 2654, (3000) Santa Fe, Argentina;* *and †Department of Chemical Engineering, University of California at Berkeley, Berkeley, California 94720*
E-mail: capesteg@fiqus.unl.edu.ar

Received July 8, 1999; accepted October 19, 1999

The effect of composition and of surface properties on alcohol-coupling reactions was studied on Mg_yAlO_x catalysts using C_2H_5OH or $^{13}CH_3OH/1\text{–}^{12}C_3H_7OH$ mixtures as reactants. Samples with Mg/Al ratios of 0.5–9.0 were obtained by thermal decomposition of precipitated hydrotalcite precursors. The nature, density, and strength of surface basic sites were obtained by temperature-programmed desorption (TPD) of CO_2 and by $^{13}CO_2/^{12}CO$ isotopic switch methods, whereas the acid site densities were measured by TPD of NH_3. The catalyst ability for activating H–H bonds was investigated by performing H_2–D_2 steady-state equilibration reactions. Isotopic tracer studies were carried out in order to probe chain growth pathways in the synthesis of isobutanol. The rates and product selectivity for C_2H_5OH or CH_3OH/C_3H_7OH reactions strongly depended on the chemical composition of Mg_yAlO_x samples. In turn, the chemical composition affected the acid–base properties of Mg_yAlO_x samples by modifying surface acid and base site densities and the distribution of strength for such sites. The rate of alcohol dehydration to ethers and olefins increased with increasing Al content. Al-rich Mg_yAlO_x samples contained a high density of $Al^{3+}-O^{2-}$ site pairs and of moderate strength basic sites, the combination of which promoted the formation of ethylene or propylene from primary alcohols via E_2 elimination pathways. The competitive dehydration to form ethers involved the adsorption of two alcohol molecules on neighboring active sites offering different acid–base properties. On Mg_yAlO_x samples, the active acid sites for ether formation were probably the Al^{3+} cations, whereas the basic sites were the neighboring O^{2-} ions. The abundance of surface Al^{3+}–O^{2-} pairs accounted for the high ether formation rates observed on Al_2O_3 and Al-rich Mg_yAlO_x samples. The dehydrogenation of alcohols to aldehydes (C_2H_4O or C_3H_6O) involved the initial alkoxy intermediate formation on weak Lewis acid–strong Brønsted base site pairs. The synthesis of C_2H_4O or C_3H_6O was favored on Mg-rich Mg_yAlO_x samples because these samples contained a much larger number of properly positioned Al^{3+} Lewis acid sites and Mg^{2+}–O^{2-} basic pairs, which are required for hydrogen abstraction steps leading to alkoxy intermediates. Pure MgO showed lower dehydrogenation rates than Mg-rich Mg_yAlO_x samples because the predominant presence of isolated O^{2-} hindered formation of alkoxy intermediates by alcohol dissociative adsorption. Aldol condensation reactions on Mg_yAlO_x samples involved also the formation of a carbanion intermediate on Lewis acid–strong Brønsted base pair sites and yielded products containing a new C–C bond such as n-C_4H_8O (or n-C_4H_9OH) and iso-C_4H_8O (or iso-C_4H_9OH). Reactions leading to condensation products were also favored on Mg-rich samples, but they took place at much slower rates than those of the corresponding dehydrogenation reactions to aldehydes. This reflected the bimolecular and consecutive character of condensation reactions, which are affected not only by the catalyst acid–base properties but also by the chemical nature of the alcohols and steric factors. © 2000 Academic Press

Key Words: **alcohol coupling reactions; Mg_yAlO_x catalysts; base–acid catalysis.**

INTRODUCTION

Copper-based catalysts are widely used to produce linear or branched higher alcohols from synthesis gas. $Cu/ZnO/Al_2O_3$ catalysts selectively form methanol from $CO/CO_2/H_2$ mixtures at low pressures (<5 MPa) and temperatures (<550 K) (1). Other methanol synthesis catalysts also promote chain growth and the formation of higher alcohols from synthesis gas. For example, Cu-Co/$ZnAl_2O_4$ catalysts give mixtures of methanol and linear C_2–C_6 alcohols (2, 3). Alkali species, especially those of Cs, increase the rate of formation of branched alcohols (4, 5). Isobutanol (2-methyl-1-butanol) is preferentially formed because it is a kinetic endpoint of aldol-coupling reactions catalyzed by basic sites on these catalysts. The synthesis of branched alcohols from H_2–CO mixtures have also been reported recently on K- and Cs-promoted $Cu_zMg_yCeO_x$ catalysts (6–8).

Isobutanol is a useful chemical and a potential precursor to isobutene and methyl-tert-butyl ether. Isobutanol synthesis requires several catalytic functions: (i) hydrogenation sites to form methanol and (ii) sites for C_1 to C_2 chain growth and C_2+ formation via different mechanisms catalyzed by basic sites aided by Cu sites (4, 9). Methanol synthesis pathways on Cu have been widely studied, and there exists general agreement about the requirement for Cu metal sites and for CO_2 as a "co-catalyst" for the reaction of H_2–CO mixtures (10, 11). Chain growth pathways

0021-9517/00 $35.00

leading to branched alcohols on metal–base catalysts are more complex, depend on the detailed catalyst composition (4, 9), and remain less clear. Specifically, identification of rate-determining steps in the overall reaction sequence for isobutanol synthesis and the specific basic sites required for such steps remain unclear.

Hydrotalcite-derived Mg–Al mixed oxides catalyze reactions requiring carbanion intermediates, such as aldol condensation reactions of aldehydes and ketones (12–14), side-chain alkylations (15), Knoevenagel condensations (16), cyanoethylation of alcohols (17), and double-bond isomerization of alkenes (18). The surface acid–base properties of Mg/Al hydrotalcites decomposed in nitrogen and their catalytic properties depend on chemical composition and on the method used to decompose the hydrotalcite precursors (14, 18, 19). Intermediate Mg/Al ratios lead to optimum catalytic properties for several reactions, but the optimum Mg/Al ratio for each reaction depends on the specific requirements for basic site density and strength. Schaper *et al.* (18) reported that Mg–Al hydrotalcites treated in air at 773 K show stronger basic sites and higher 1-pentene double-bond migration rates than pure MgO. Corma *et al.* (19) observed maximum isopropanol dehydrogenation rates on air-treated hydrotalcites with an Mg/Al ratio of 3. The rate of self-condensation of acetone to α,β-unsaturated ketones reaches a maximum on Al-rich samples ($Mg/Al < 1$) (14), apparently as a result of contributions from aldol condensation pathways catalyzed by both basic and acidic sites.

In a previous study (20), we examined the structural purity, site density, surface composition, and acid–base properties of Mg–Al catalysts prepared by decomposition of hydrotalcite precursors in nitrogen. Here, we describe the effect of composition and of surface properties on alcohol coupling reactions, using C_2H_5OH or $^{13}CH_3OH$/1-$^{12}C_3H_7OH$ as reactants. The objectives of these kinetic and isotopic tracer studies were to establish the reaction steps required for alcohol chain growth and to ascertain the sites and structures required for the efficient catalysis of such steps.

The nature, density, and strength of acid and basic sites are probed by temperature-programmed desorption of NH_3 and CO_2 coupled with infrared spectra of adsorbed CO_2. On Mg–Al mixed oxides, both the surface acid–base properties and the catalytic activity and selectivity depend on chemical composition. Mg-rich samples form predominantly aldehydes via dehydrogenation reactions, whereas Al-rich catalysts favor dehydration to ethers. Coupling products are formed via consecutive aldol condensation steps from aldehydic intermediates. Dehydration, dehydrogenation, and coupling reactions proceed through different mechanisms and require different surface active sites. The effect of chemical composition on the selectivity of Mg_yAlO_x samples is interpreted in terms of changes in the relative abundance of basic and acid sites required for chain growth pathways.

EXPERIMENTAL

1. *Catalyst Preparation*

Mg–Al hydroxycarbonate precursors with Mg/Al atomic ratios (y) of 0.5, 1, 5, and 9 were prepared by coprecipitation. An acidic solution of the metal nitrates with a total $[Al + Mg]$ cation concentration of 1.5 M was contacted with an aqueous solution of KOH and K_2CO_3 at a constant pH of 10. The two solutions were simultaneously added dropwise to 300 ml distilled water kept at 333 K in a stirred batch reactor. The resulting precipitates were aged for 2 h at 333 K in their mother liquor and then filtered, washed thoroughly with 300–500 ml deionized water at 373 K, and dried at 348 K overnight. The residual potassium content in all dried samples was below 0.1 wt%. Hydrotalcite precursors were decomposed in N_2 at 673 K for 4 h in order to obtain the corresponding Mg–Al mixed oxides (Mg_yAlO_x). Pure MgO and Al_2O_3 were prepared following the same procedure.

2. *Catalyst Characterization*

The crystalline phases in the precipitated hydrotalcites before and after decomposition were determined by X-ray diffraction (XRD) using a Shimadzu XD-Dl diffractometer and Ni-filtered Cu Kα radiation. BET surface areas (S_g) were measured by N_2 physisorption at its boiling point using a Quantachrome Nova-1000 sorptometer. Elemental compositions were measured by atomic absorption spectroscopy (AAS).

CO_2 adsorption site densities and binding energies were obtained from temperature-programmed desorption (TPD) of CO_2 preadsorbed at room temperature. Samples (50 mg) were treated in He ($\sim$100 cm^3/min) at 723 K for 0.3 h and exposed to 0.1% CO_2/0.1% Ar/He (Cambridge Isotope Laboratories Inc.) for 0.15 h at room temperature (RT). Weakly adsorbed CO_2 was removed by flowing He at RT, and the temperature was then increased to 723 K at 30 K/min. CO_2 concentrations in the effluent were measured by mass spectrometry (MS).

Basic site densities were also measured by $^{13}CO_2$/$^{12}CO_2$ isotopic switch methods that give the number of sites available for reversible adsorption–desorption of CO_2 at typical reaction temperatures, as described in detail elsewhere (8, 20). Samples were exposed to a 0.1% $^{13}CO_2$/0.1% Ar/He (Cambridge Isotope Laboratories, Inc.) stream at 573 K until $^{13}CO_2$ reached a constant concentration in the effluent (0.5 h). Then, the flow was switched to 0.1% $^{12}CO_2$/He (Cambridge Isotope Laboratories, Inc.). The resulting decrease in the surface concentration of $^{13}CO_2$, as it was replaced by $^{12}CO_2$, was followed by mass spectrometric analysis of $^{13}CO_2$ and Ar concentrations in the effluent stream as a function of the time elapsed after the isotopic switch. Ar was used as an internal standard in order to correct for gas holdup and hydrodynamic delays within the apparatus.

Acid site densities were measured by TPD of NH_3 preadsorbed at room temperature. Samples (150 mg) were treated in He (∼100 cm^3/min) at 723 K for 0.5 h and exposed to a 0.93% NH_3/He stream until saturation coverages were reached. Weakly adsorbed NH_3 was removed by flowing He at RT for 0.5 h. Temperature was then increased to 773 K at 10 K/min, and the NH_3 concentration in the effluent was measured by mass spectrometry.

3. *Catalytic Reactions*

3.1. H_2–D_2 steady-state equilibration reaction on Mg_yAlO_x. H_2–D_2 equilibration reactions were carried out in a differential packed bed reactor. Decomposed hydrotalcite samples (150 mg) were treated in flowing He (∼100 cm^3/min) at 723 K for 0.5 h. Then, an $H_2/D_2/Ar$ (5%/5%/90%) mixture was introduced at 105 cm^3/min while the sample was at room temperature, and the temperature was increased at 10 K/min to 773 K. H_2, D_2, and HD concentrations in the effluent were measured continuously by mass spectrometry. Calibrations for H_2, HD, and D_2 were obtained from the signals at 2, 3, and 4 amu using the reactant mixture and an isotopically equilibrated mixture as standards.

3.2. Reactions of ethanol on Mg_yAlO_x. Ethanol reactions were carried out in a differential fixed-bed reactor at 573 K and atmospheric pressure. Samples were sieved to retain particles with 0.35–0.42 mm diameter for catalytic measurements and treated in N_2 at 673 K for 1 h before reaction in order to remove adsorbed H_2O and CO_2. C_2H_5OH (Merck, ACS, 99.8% purity) was introduced via a syringe pump and vaporized into flowing N_2 to give a N_2/C_2H_5OH molar ratio of 10. Reaction rates and selectivities were independent of particle size in the range between 0.15 and 0.59 mm; thus, diffusional restrictions do not corrupt measured reaction rates. Reaction rates are defined on an areal basis as the moles of ethanol converted per unit of time and per unit of BET surface area. Catalytic tests were conducted at contact times ($W/F^0_{C_2H_5OH}$) between 4 and 120 g h/mol C_2H_5OH. The concentrations of unreacted C_2H_5OH and of reaction products in the reactor effluent were measured at 0.5-h intervals for 10 h using an ATI Unicam 610 chromatograph equipped with a 0.2% Carbowax 1500/80-100 Carbopack C column and flame ionization detection.

3.3. Cross-coupling reactions of $^{13}CH_3OH$/1–$^{12}C_3H_7OH$ mixtures on Mg_yAlO_x. Cross-coupling reactions of $^{13}CH_3OH$ (^{13}C, 99%; ^{18}O, <1%; Icon Services Inc.) with unlabeled 1-C_3H_7OH (Aldrich, 99.7%) were carried out in a gradientless recirculating batch reactor, at atmospheric pressure (21). Samples (38.0 mg) were treated in vacuum by heating to 723 K at 3.5 K/min and holding for 2 h. The temperature was then decreased to 573 K, and the reactants were introduced along with a small amount of methane (used as an inert internal standard in order to ensure accurate mass balances). Reactant mixtures consisting of $^{12}C_3H_7OH/^{13}CH_3OH/CH_4/He$ (1.4/2.7/2.7/94.5 kPa) were circulated continuously through the catalyst bed at about 300 cm^3/min. The circulating stream was sampled after various contact times by syringe extraction. Reactants and products were analyzed using a dual-detector gas chromatograph (Hewlett-Packard, Model 5890 II Plus; FID/TCD detectors). Gas samples were analyzed by flame ionization after separation with a 5% phenyl methyl-silicone capillary column (HP-1, 50 m, 0.32 mm diameter, 1.05 μm film thickness) and by thermal conductivity after separation in a Porapak Q packed column (1.8-m length, 0.32-cm diameter). Mass spectrometry was used after chromatographic separations in order to confirm the chemical identity of individual chromatographic peaks and to measure the number and position of ^{13}C within reactants and products (Hewlett-Packard, Model 5890 II Plus GC; Hewlett-Packard, Model 5972 Mass Selective Detector). The ^{13}C content and the isotopomer distributions of reactants and products were obtained from mass spectrometry data using matrix deconvolution methods that account for natural ^{13}C abundance and for mass fragmentation patterns (22).

RESULTS AND DISCUSSION

1. *Catalyst Characterization*

The precipitated hydrotalcite precursors showed diffraction patterns consistent with the presence of a crystalline hydrotalcite structure (ASTM 14-191). The diffraction pattern for the sample with an Mg/Al ratio of 9 also showed an additional $Mg(OH)_2$ phase (ASTM 7-239).

The physiochemical properties of the hydrotalcite samples after decomposition at 673 K are shown in Table 1,

TABLE 1

Composition, Surface Area, and XRD Characterization of Mg_yAlO_x Samples

Sample	Composition[a] Al/(Al + Mg) (molar)	BET surface area (m^2/g)	Phases detected by XRD
MgO	0.00	191	MgO
Mg_9AlO_x	0.11	114	MgO
Mg_5AlO_x	0.18	184	MgO
Mg_1AlO_x	0.47	231	MgO
$Mg_{0.5}AlO_x$	0.65	298	MgO + $MgAl_2O_4$
Al_2O_3	1.00	388	amorphous

[a] Bulk composition measured by AAS.

which includes chemical composition, BET surface area, and crystalline phases for MgO, Al_2O_3, and Mg_yAlO_x samples. The Al/(Al + Mg) atomic ratios are very similar to those present in the precursor solution, suggesting that Mg and Al salts precipitate completely during synthesis. X-ray diffraction patterns show the presence of a poorly crystalline MgO periclase phase in all the Mg_yAlO_x samples prepared by decomposition of hydrotalcite precursors. The $Mg_{0.5}AlO_x$ sample contains an additional $MgAl_2O_4$ spinel phase, but crystalline AlO_x phases were not detected in any of the Mg_yAlO_x samples.

Mg–Al hydroxycarbonate precursors evolve CO_2 and H_2O during thermal decomposition; this rapid gas evolution leads to the formation of a well-connected network of small pores with significant surface area (100–300 m^2/g). The intimate contact between Mg and Al cations in the hydrotalcite structure is preserved during decomposition and leads to the formation of well-mixed Mg_yAlO_x binary oxides. Their surface areas increase with increasing Al content, apparently because the carbonate content and thus the amount of CO_2 formed during decomposition are proportional to the Al content (23).

Basic site densities measured by $^{13}CO_2/^{12}CO_2$ isotopic exchange at 573 K on MgO, Al_2O_3, and Mg_yAlO_x samples are shown in Table 2. These measurements reflect the number of adsorption sites that can bind CO_2 reversibly at typical temperatures of catalytic reactions. This method does not count basic sites that are strong enough to bind CO_2 irreversibly at this temperatures or sites that bind molecules too weakly and desorb CO_2 with characteristic times shorter than those detected in these measurements ($\sim$2 s). The surface density (per m^2) and the total number (per g) of sites capable of reversible CO_2 chemisorption are higher on pure MgO than on Mg_yAlO_x samples and very low on pure Al_2O_3 (Table 2). Small amounts of Al decrease the density of kinetically accessible active sites in MgO; MgO adsorbs 0.38 μmol CO_2/m^2, but sample Mg_9AlO_x with only 6.2% wt Al adsorbs 0.17 μmol CO_2/m^2. X-ray photoelectron spectroscopy showed significant Al surface enrichment in Mg_yAlO_x samples with low Al/(Al + Mg) ratios (<0.20) (20). The presence of more electronegative amorphous AlO_x domains or isolated species on MgO blocks CO_2 adsorption sites, and it is likely to account for the strong effect of Al on the density of surface sites. At higher Al/(Al + Mg) ratios (0.2–0.5), the nucleation of a separate stable Al-rich phase provides a thermodynamic sink for Al^{3+} cations, and the density of basic sites increases as Al migrates from MgO surfaces to the Al-rich phase to reach a second maximum for the Mg_1AlO_x sample.

In this composition range, the Al^{3+} cations located in the MgO framework create a defect in order to compensate the positive charge generated, and the adjacent oxygen anions become coordinatively unsaturated; as a result, the solid solution displays higher basicity. In Al-rich samples (sample $Mg_{0.5}AlO_x$), the nucleation of a separate bulk $MgAl_2O_4$ spinel lacking basic surface oxygens causes the basic site density to decrease again at higher Al contents. We have also observed this decrease in basic site density at high Al contents by XPS, and chemisorption and TPD of CO_2 (20), as also reported by others (24, 25) for a more narrow compositional range.

The distribution of binding sites with basic properties was determined by temperature-programmed desorption (TPD) of CO_2 preadsorbed at RT on MgO, Mg_yAlO_x, and Al_2O_3. The TPD profile for Mg_1AlO_x (Fig. 1) shows that CO_2 desorbs in three overlapping peaks, as also observed on all other samples except Al_2O_3. These features are referred to as α- (low-temperature), β- (intermediate temperature), and γ- (high-temperature) peaks in the discussion that follows. The relative contributions from these three

TABLE 2

Catalyst Characterization: Acid–Base Properties

		Temperature-programmed desorption of CO_2 and NH_3						
		Areas under CO_2 TPD peaks[b] ($\mu mol/m^2$)				Areas under NH_3 TPD peaks ($\mu mol/m^2$)		
Catalyst	Exchangeable CO_2 at 573 K[a] ($\mu mol/m^2$)	α[c]	β[c]	γ[c]	Total evolved CO_2 ($\mu mol/m^2$)	B[d]	L[d]	Total evolved NH_3 ($\mu mol/m^2$)
MgO	0.38	0.06(3.5)	0.32(19.8)	1.25(76.7)	1.63	0.18	0.30	0.48
Mg_9AlO_x	0.17	0.23(20.0)	0.44(37.3)	0.50(42.7)	1.17	0.49	0.32	0.81
Mg_5AlO_x	0.18	0.08(16.7)	0.17(37.6)	0.21(45.7)	0.46	0.21	0.64	0.84
Mg_1AlO_x	0.33	0.18(21.9)	0.37(44.5)	0.28(33.6)	0.83	0.53	1.04	1.57
$Mg_{0.5}AlO_x$	0.17	0.17(23.2)	0.32(44.2)	0.24(32.6)	0.73	0.42	0.97	1.39
Al_2O_3	0.04	0.16(48.6)	0.18(51.4)	0.00(0.0)	0.34	0.50	0.84	1.34

[a] Measured by the $^{13}CO_2/^{12}CO_2$ isotopic switch method.

[b] Parenthesis are the percentage of contribution of each peak.

[c] α, low-temperature peak; β, middle-temperature peak; γ, high-temperature peak.

[d] B, Brønsted peak; L, Lewis peak.

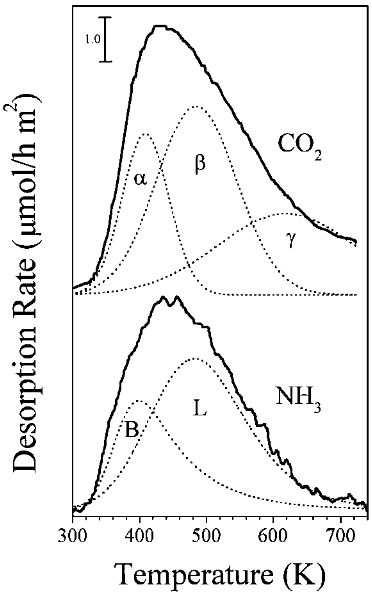

FIG. 1. TPD profiles of CO_2 and NH_3 on Mg_1AlO_x. Deconvolution of CO_2 TPD trace: α, low-temperature peak; β, middle-temperature peak; γ, high-temperature peak. Deconvolution of NH_3 TPD trace: B, Brønsted peak; L, Lewis peak. Heating rates: 30 K/min (CO_2 TPD), 10 K/min (NH_3 TPD).

types of adsorbed CO_2 were obtained by deconvolution of the experimental TPD profiles and integration of the three desorption features. Although CO_2 desorption follows a first-order kinetics, we have used for simplicity Gaussian functions for the deconvolution of the TPD traces. The adsorbed CO_2 surface densities are shown in Table 2 for all samples.

The complex TPD profiles suggest that MgO and Mg_yAlO_x surfaces are nonuniform and contain several types of adsorbed CO_2. Infrared spectra of CO_2 adsorbed on MgO and Mg_yAlO_x (20) detected three distinct adsorbed structures, located on surface sites with different structures and basic strengths. Bicarbonates form on weakly basic OH groups, bidentate carbonates adsorb on Mg–O site pairs with accessible cations, and unidentate carbonates on strongly basic surface O^{2-} anions. These combined IR and TPD data led us to assign the desorption peaks to CO_2 species adsorbed on OH groups (α-peak), Mg-O pairs (β-peak), and O^{2-} anions (γ-peak). With this assignment, the data on Table 2 show that pure MgO contains the highest absolute (1.25 μmol CO_2/m^2) and relative (76.7%) amounts of strongly basic O^{2-} sites. The relative concentration of surface OH groups and Mg–O pairs in Mg_yAlO_x increases with increasing Al content, leading to a net decrease in the average basic strength of surface sites. Al_2O_3 is an amphoteric oxide and lacks strong basic sites, but it contains surface sites capable of binding CO_2 with low and medium binding energy, corresponding to surface OH groups and Al–O site pairs. Weakly bonded bicarbonate species desorb at low temperatures and do not account for the adsorbed CO_2 detected by isotopic exchange methods at 573 K. This explains the low basic site density obtained from exchange measurements on Al_2O_3 (0.04 $\mu mol/m^2$; column 2 in Table 2). The total amount of CO_2 evolved during TPD (column 6 in Table 2) follows compositional trends similar to those observed for the kinetically accessible adsorbed CO_2 measured by isotopic exchange. The total surface density of adsorbed CO_2 from TPD decreases from a maximum value on MgO (1.63 $\mu mol/m^2$) to a minimum value as small amounts of Al are added, and then it increases to a second maximum (0.83 $\mu mol/m^2$) on the Mg_1AlO_x sample.

The acid properties of MgO, Mg_yAlO_x, and Al_2O_3 surfaces were probed by TPD of NH_3 preadsorbed at room temperature. Previous work by Shen *et al.* (26) on the NH_3 adsorption on Mg–Al mixed oxides showed that Mg_yAlO_x samples contain Brønsted and Lewis acid sites. These authors assigned the Lewis acid sites to Al–O–Mg species located within a MgO structure and containing the Al^{3+} cations predominantly in octahedral sites. NH_3 adsorption on Lewis sites is stronger than on Brønsted acid sites provided by surface OH groups. Lewis acid sites adsorb NH_3 by coordinating the nitrogen free electron pair with Mg and Al cations, whereas on Brønsted sites a surface proton is donated to NH_3 with formation of NH_4^+. In agreement with the results obtained by Shen *et al.* (26), the NH_3 TPD profile on Mg_1AlO_x (Fig. 1) shows that NH_3 desorbs in two overlapping peaks, as also observed for all other Mg_yAlO_x samples and pure MgO and Al_2O_3. The low- (B-peak) and high-temperature (L-peak) peaks are assigned to Brønsted and Lewis surface acidic sites, respectively. The NH_3 surface densities for Brønsted and Lewis sites were obtained by deconvolution and integration of the TPD traces and are presented in Table 2, column 9. The total adsorbed NH_3 surface density is low on MgO and Mg-rich samples, but it increases with increasing Al content reaching a maximum at 1.57 $\mu mol/m^2$ for the Mg_1AlO_x sample. The density of Lewis acid sites, consisting of Mg^{2+} cations on pure MgO, increases from 0.30 $\mu mol/m^2$ on MgO to about 1.00 on Al-rich Mg_yAlO_x samples (Table 2, column 8). Pure MgO exhibits the lowest density of Brønsted acid sites (Table 2, column 7).

2. *H_2–D_2 Steady–State Equilibration Reactions on MgO, Al_2O_3, and Mg_yAlO_x Catalysts*

The isotopic equilibration of gaseous H_2–D_2 mixtures, as well as the exchange of gas–phase D_2 with surface H, have been employed for investigating the surface reactivity, state, and content of surface hydrogen either on mixed oxides (27, 28) or on metallic catalysts (29).

Here, H_2–D_2 isotopic equilibration reactions were used in order to explore the ability of Mg–Al oxides to activate H–H bonds. Areal H_2–D_2 equilibration rates (r_{HD}, μmol/min m^2) were measured as a function of temperature on MgO, Al_2O_3, and Mg_yAlO_x samples, and the obtained r_{HD}

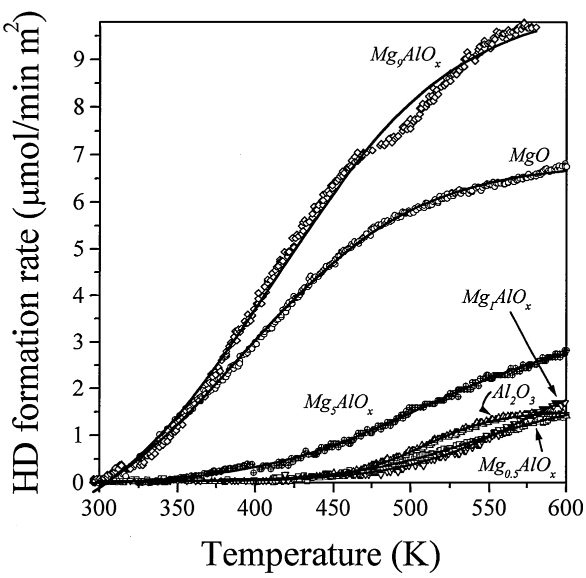

FIG. 2. HD formation rate for H_2–D_2 equilibration reactions as a function of temperature on MgO, Al_2O_3, and Mg_yAlO_x samples [$P=101.3$ kPa, $H_2:D_2:Ar=5:5:90$, $W/F^0_{D_2}=11.6$ g h/mol, heating rate $=10$ K/min].

vs T sigmoid-shaped curves are shown in Fig. 2. Magnesium-rich samples (MgO and Mg_9AlO_x) are clearly more active than samples with the highest Al content (Mg_1AlO_x, $Mg_{0.5}AlO_x$, and Al_2O_3). At the temperature of our alcohol conversion catalytic studies reported below (573 K), the Mg_9AlO_x sample gave the highest H_2–D_2 equilibration rate.

H_2–D_2 equilibration rates depend on the surface concentration of H and D and on the distance away from isotopic equilibrium (30). For Langmuir–Hinshelwood mechanisms via dissociative H_2 and D_2 adsorption, the HD formation rate for a 5% D_2/5% H_2/Ar reactant mixture is given by

$$H_2 + D_2 \Leftrightarrow 2HD$$

$$r_{HD} = k_s\left[P^{0.5}_{H_2}P^{0.5}_{D_2} - P_{HD}/K^{0.5}\right] = 0.05\,k_s\left[1 - 2X_{D_2}\right], \quad [1]$$

where k_s (μmol/atm min m^2) is the apparent first-order kinetic constant per unit of surface area, K is the equilibrium constant ($K \approx 4$ throughout the experimental temperature range), and X_{D_2} is the D_2 conversion. From the design equation for an isothermal plug–flow reactor, we obtain

$$\frac{W}{F^0_{D_2}} = \int_0^{X_{D_2}} \frac{dX_{D_2}}{0.5S_g r_{HD}} = \int_0^{X_{D_2}} \frac{dX_{D_2}}{0.025S_g k_s(1 - 2X_{D_2})}. \quad [2]$$

The k_s values on all catalysts were obtained by integrating Eq. [2] using rate data obtained at X_{D_2} values lower than 0.1. Figure 3 shows the values of k_s as a function of composition at 348, 373, and 398 K. Rate constants on MgO and Mg_9AlO_x samples are about three orders of magnitude larger than on the Al-rich samples (Mg_1AlO_x, $Mg_{0.5}AlO_x$, and Al_2O_3). These results are consistent with previous reports, which have shown that the activation energy for H_2/D_2 equilibration on Al_2O_3 is significantly higher than on MgO (31, 32).

Pure MgO and Al_2O_3 catalyze H_2–D_2 equilibration at low temperatures (27, 28) but show negligible catalytic activity after complete surface dehydroxylation (33, 34), thereby suggesting that surface hydrogen stabilized at OH groups participates in the exchange reaction. Nakano *et al.* (35), proposed that the active sites on MgO are Mg–O pairs, which dissociate H_2 heterolytically to form magnesium hydride and H^+ species in surface OH groups. Boudart *et al.* (33) proposed instead that active sites on MgO consist of electron-deficient paramagnetic centers vicinal to surface OH groups with no direct participation of metal cations. These later authors showed that for temperatures lower than 300 K, pure MgO catalyzes the H_2–D_2 equilibration reaction but is almost inactive for exchanging surface hydrogen with gas-phase D_2. In the case of alumina, Kazansky *et al.* (36) proposed that the heterolytic H_2 dissociation occurs on unstable Al^+–O^- pairs with subsequent formation of surface aluminum hydrides. They also showed that at temperatures lower than 300 K Al_2O_3 catalyzes H–D exchange reactions, but it does not dissociate H_2 significatively. From previous reports and the results described above, it appears that the higher activity of Mg-rich samples in H_2–D_2 equilibration reactions (Fig. 3) reflects the higher rate of H_2 dissociation on Mg–O. The role of surface hydroxyl groups in H_2–D_2 equilibration on partially dehydroxylated materials is probably to promote the migration of adsorbed H(D) species from $H_2(D_2)$ dissociation to form HD by recombination of hydrogen atoms

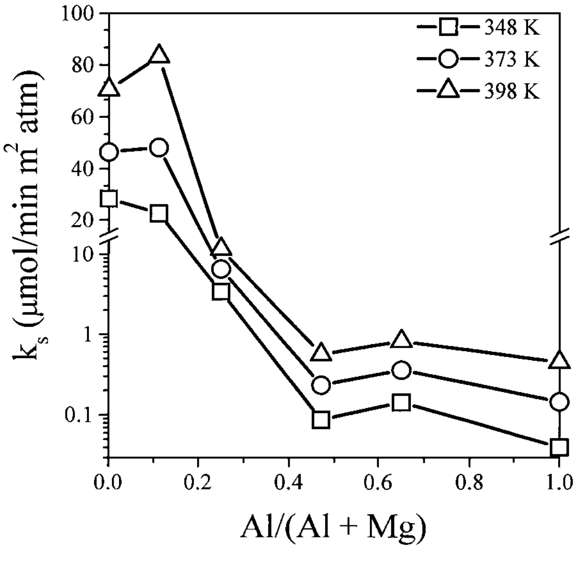

FIG. 3. Apparent kinetic constant k_s for H_2–D_2 equilibration reactions as a function sample composition. The k_s were obtained by integrating Eq. [2] using D_2 conversion values lower than 0.1 (see text).

dissociated on separate dissociation sites. A proper combination of $H_2(D_2)$ dissociation sites and H–D exchange sites would then enhance the catalyst activity for H_2–D_2 equilibration reactions. Thus, the Mg_9AlO_x sample displays the highest H_2–D_2 equilibration rate probably because of an optimum balance between the number of surface Mg–O pairs and surface OH groups

3. *Ethanol Reaction Rates and Pathways on MgO, Al_2O_3, and Mg_yAlO_x Catalysts*

Dehydrogenation and coupling reactions of ethanol (C_2H_5OH) on mixed oxides form many products and proceed via complex reaction pathways that may require specific combinations of acid and basic sites. The predominant products of ethanol reactions on Mg–Al oxides were acetaldehyde (C_2H_4O), *n*-butanol (*n*-C_4H_9OH), diethylether ($C_2H_5OC_2H_5$), and ethylene (C_2H_4). Minor amounts of *n*-butyraldehyde (*n*-C_4H_8O), ethyl acetate ($CH_3COOC_2H_5$), and 2-propanol (2-C_3H_7OH) were also formed on MgO and Mg_yAlO_x catalysts with low Al content. Other coupling products, such as acetone (CH_3COCH_3) and 2-pentanone ($CH_3COCH_2CH_2CH_3$), were detected only in trace amounts. Diethylether and ethylene were the only products detected on the pure Al_2O_3 sample.

Ethanol conversion rates decreased with time-on-stream on both MgO and Mg_yAlO_x samples (to ∼50% of initial rates after 10 h), but no deactivation was observed on the Al_2O_3 sample. Figure 4 shows ethanol conversions ($X_{C_2H_5OH}$) and product yields (η_i; mol of product *i*/mol of ethanol in feed) on Mg_1AlO_x as a function of time-on-stream. Diethyl-ether and *n*-butanol were the main products formed on Mg_1AlO_x; significant amounts of C_2H_4 and C_2H_4O, as well as minor amounts of ethyl acetate, were also observed. Formation of *n*-C_4H_8O was detected only initially on this sample.

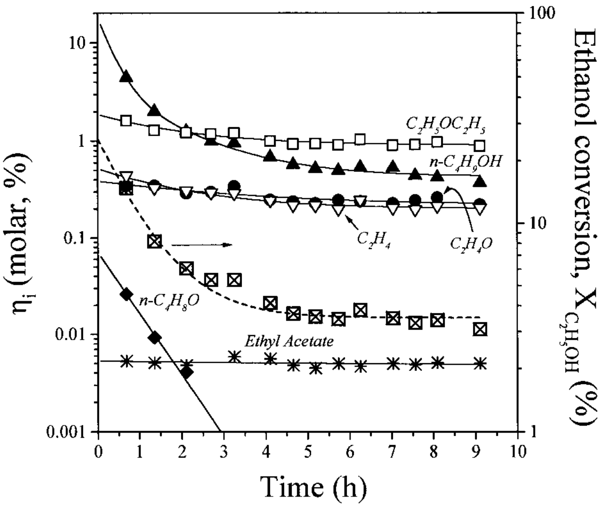

FIG. 4. Product distribution for ethanol conversion reactions on Mg_1AlO_x. Product yields (η_i) and ethanol conversion ($X_{C_2H_5OH}$) as a function of time [573 K, 101.3 kPa total pressure, N_2/ethanol = 10, $W/F^0_{C_2H_5OH} = 46$ g h/mol].

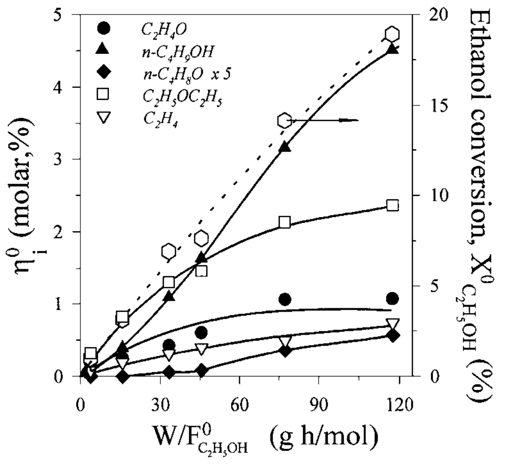

FIG. 5. Product distribution for ethanol conversion reactions on Mg_1AlO_x. Initial product yields (η_i^0) and ethanol conversion ($X^0_{C_2H_5OH}$) as a function of contact time [573 K, 101.3 kPa total pressure].

The effect of contact time on the product distribution on Mg_1AlO_x was determined in order to identify primary and secondary reaction pathways. The observed deactivation, however, required that each data point be obtained on a fresh catalyst and that initial product yields be obtained by extrapolating to initial time-on-stream using semi-logarithmic plots. These initial yields, η_i^0, and the corresponding initial ethanol conversion values are shown as a function of contact time in Fig. 5. The local slopes of the curves in Fig. 5 give the rate of formation of each product at a specific ethanol conversion and residence time. The nonzero initial slopes for acetaldehyde, diethylether, and ethylene show that they form directly from ethanol via dehydrogenation, coupling followed by dehydration, and dehydration reactions, respectively. Diethylether and ethylene yields increase monotonically with increasing residence time, because they react slowly in secondary reactions, but acetaldehyde reaches a maximum concentration as it converts to larger oxygenates in secondary condensation reactions with increasing residence time. The initial zero slope of the *n*-butyraldehyde yield curve is consistent with its formation via the secondary condensation of primary acetaldehyde products. *n*-Butanol becomes the predominant product at longer contact times. The sigmoidal shape of the *n*-butanol yield curve (Fig. 5) and its low but nonzero initial slope suggest that *n*-butanol forms via two or more parallel pathways, such as direct condensation of ethanol and sequential paths involving hydrogenation of the *n*-butyraldehyde formed via acetaldehyde condensation steps. Ethyl acetate was also detected in low concentrations among reaction products (yield curves not shown in Fig. 5).

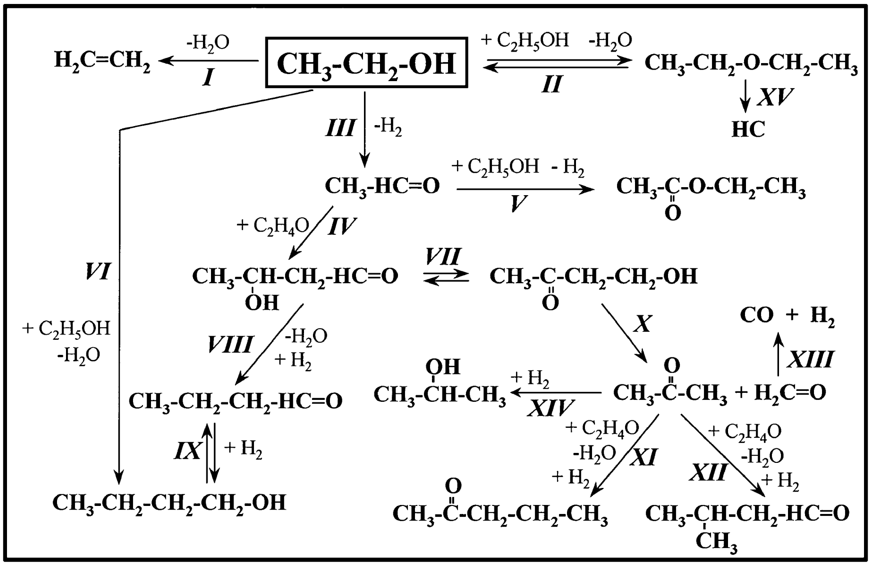

FIG. 6. Reaction network for ethanol conversion reactions.

These results and previous literature reports (4, 8, 20, 37, 38) lead us to propose the reaction network described in Fig. 6. In this scheme, ethanol is converted on Mg_yAlO_x samples predominately via dehydrogenation, aldol coupling, and dehydration reactions. Acetaldehyde forms via ethanol dehydrogenation (step III). Aldol intermediates formed from acetaldehyde condensation (step IV) dehydrate to form α,β-unsaturated aldehydes (crotonaldehyde), which rapidly hydrogenate to *n*-butyraldehyde (step VIII) using H_2 formed in ethanol dehydrogenation steps. This aldol intermediate can also decompose to acetone or 2-propanol via reverse aldol coupling (steps X and XIV) after an intramolecular hydride shift leading to the keto form (step VII) (8). *n*-Butanol can form via direct condensation of ethanol (8) (step VI) or by hydrogenation of *n*-butyraldehyde (step IX), but the latter pathway is thermodynamically unfavored at the low H_2 concentrations prevalent during ethanol reactions. Ethylene is formed by monomolecular dehydration of ethanol (step I). Diethylether is formed in bimolecular dehydration steps (step II), and it can react further to form alkanes and alkenes (step XV) on acid sites, using pathways similar to those reported for dimethylether and methanol conversion to hydrocarbons. Ethylacetate forms via Tischenko-type reactions between aldehydic and alkoxide adsorbed species (step V) (39, 40).

4. Reaction Pathways of $^{13}CH_3OH/1\text{–}^{12}C_3H_7OH$ Mixtures on MgO, Al_2O_3, and Mg_yAlO_x Samples

Isotopic tracer studies using $^{13}CH_3OH/1\text{–}^{12}C_3H_7OH$ mixtures were carried out in order to probe chain-growth pathways involved in the synthesis of higher alcohols, especially isobutanol (2-methyl-1-propanol) on Mg_yAlO_x. Product yields ($\eta_i = n_i/n_T^0$, where n_i is the moles of product i and n_T^0 is the total initial moles of reactants) are shown in Fig. 7 for Mg_1AlO_x as a function of Wt/n_T^0, where W is the catalyst weight and t the reaction time. The local slope for each product in Fig. 7 gives its rate of formation at a specific value of reactant conversion and contact time. The predominant reaction products are propionaldehyde (C_3H_6O), methyl-propyl ether ($CH_3OC_3H_7$), isobutanol (iso-C_4H_9OH), dimethyl ether (CH_3OCH_3), propylene (C_3H_6), di-*n*-propyl ether ($C_3H_7OC_3H_7$), and isobutyraldehyde (iso-C_4H_8O). Other minor products are methyl

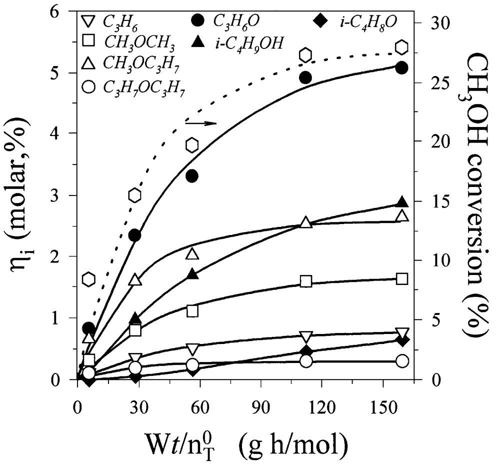

FIG. 7. Product distribution for reactions of $^{13}CH_3OH/1\text{–}^{12}C_3H_7OH$ mixtures. Product yields and methanol conversions as a function of parameter Wt/n_T^0. Recirculating reactor data for Mg_1AlO_x catalyst [573 K, 101.3 kPa total pressure, $W = 0.038$ g, 2.7 kPa methanol, 1.4 kPa 1-propanol, balance He].

propionate, butenes, 2-methyl-1pentanol (iso-$C_5H_{11}OH$), and 3-pentanone ($C_2H_5(CO)C_2H_5$).

On Mg_1AlO_x, propionaldehyde was the main reaction product; dehydrogenation reactions occurred faster than dehydration or chain growth. The nonzero initial slopes for C_3H_6O, $CH_3OC_3H_7$, CH_3OCH_3, C_3H_6, and $C_3H_7OC_3H_7$ show that these products form directly from the methanol and 1-propanol reactants. Isobutyraldehyde yields, however, show a zero initial slope. As in the case of 1-butanol formation from ethanol (Fig. 5), the low but nonzero initial slope for isobutanol formation from 1-propanol/methanol mixtures (Fig. 7) suggests that the reaction involves parallel paths. In this case, such paths include the direct condensation of methanol-derived surface intermediates with 1-propanol and/or with the propionaldehyde formed in primary 1-propanol dehydrogenation reactions.

The ^{13}C-content in 1-propanol and methanol and in the major products of their reactions was measured by mass spectrometry after chromatographic separation using a capillary column. The measured isotopic contents in reaction products formed on Mg_1AlO_x are shown in Table 3. The results of these isotopic tracer studies (Table 3) confirmed the reaction sequence described in Fig. 8 and previously inferred from the observed effects of residence time on product yields (Fig. 7).

1-Propanol and all reaction products derived directly from 1-propanol are predominantly unlabeled (Table 3). Propionaldehyde forms by dehydrogenation of 1-$^{12}C_3H_7OH$ (step VIII) and shows no detectable ^{13}C-enrichment. Di-*n*-propyl ether is also mainly unlabeled, and it forms by bimolecular dehydration reactions of 1-$^{12}C_3H_7OH$ (step IV). Propylene shows only about 1% ^{13}C enrichment, as expected from its formation via monomolecular dehydration of 1-$^{12}C_3H_7OH$ (step I). The small amounts of 2-methyl-1-pentanol formed by self-condensation of 1-$^{12}C_3H_7OH$ (steps XIII, XIV, and XV) also do not show ^{13}C contents above natural abundance.

TABLE 3

^{13}C-Distribution in Reactants and Products of $^{13}CH_3OH$–C_3H_7OH Reactions on Mg_1AlO_x

	Number of ^{13}C (%)				
Compound	0	1	2	3	4
CH_3OH	1.9	98.1	—	—	—
C_3H_7OH	98.1	1.6	0.0	0.3	—
C_3H_6O	99.8	0.2	0.0	0.0	—
iso-C_4H_9OH	4.7	94.6	0.4	0.3	0.0
iso-C_4H_8O	5.8	94.2	0.0	0.0	0.0
$CH_3OC_3H_7$	1.5	98.0	0.4	0.0	0.0
CH_3OCH_3	0.0	10.6	89.4	—	—
$C_3H_7OC_3H_7$	98.0	1.3	0.7	0.0	0.0
C_3H_6	98.0	1.0	1.0	0.0	—

Note. 573 K, 101.3 kPa total pressure, 2.7 kPa methanol, 1.4 kPa 1-propanol, balance He, 2.8 h reaction time.

The presence of ^{13}C in the other reaction products shows that they involve $^{13}CH_3OH$ as a reactant. Dimethylether molecules contain predominantly two ^{13}C-atoms ($^{13}CH_3O^{13}CH_3$), because they form via dehydration of $^{13}CH_3OH$ (step II). The identity of the $^{13}C_1$ intermediate required is unclear, and adsorbed formyl or methoxy

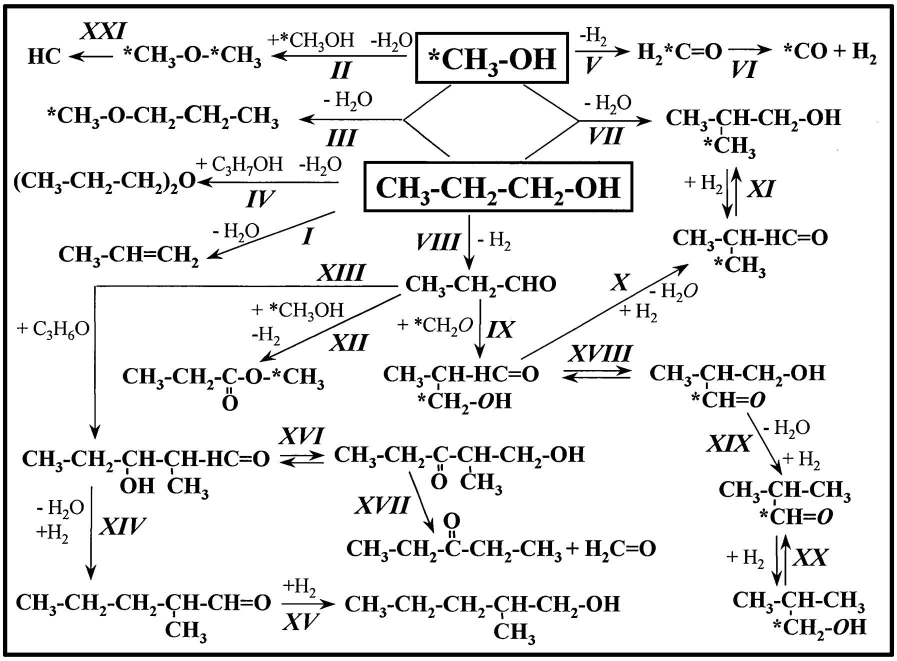

FIG. 8. Reaction network for methanol/1-propanol reactions.

species and gas-phase formaldehyde have been proposed (8). We did not detect formaldehyde among reaction products because of its high reactivity, but the presence of ^{13}CO among products suggests that $^{13}CH_3OH$ dehydrogenation to $H_2{}^{13}CO$ is likely to occur as an intermediate step in the decarbonylation of methanol to ^{13}CO (steps V and VI). Some dimethylether molecules (about 10%, Table 3) contain only one ^{13}C; this is higher than expected from the number of methanol precursors with ^{12}C. It appears that unlabeled methanol and singly labeled dimethylether can also form via a $^{12}C_1$ intermediate derived from C–C bond cleavage in aldol intermediates formed from two $^{12}C_3H_6O$, after the latter undergo intramolecular hydrogen transfer (aldol-keto isomerization) and reverse aldol reactions (steps XIII, XVI, and XVII).

When products form via cross-coupling reactions, the position of the ^{13}C-atom can reveal mechanistic details not available from the ^{13}C-content alone. The most abundant cross-coupling products were methyl-propyl ether, isobutyraldehyde, and isobutanol. The single ^{13}C in methyl-propyl ether was located at the methyl carbon and directly bonded to the ether linkage, as expected from the bimolecular dehydration of 1-propanol and methanol (step III).

Isobutyraldehyde and isobutanol contained predominantly one ^{13}C (94.2%, 94.6%; Table 3). Their similar ^{13}C-contents suggest that they arise from a common reaction intermediate, which in turn forms via condensation reactions of one C_1 species derived from $^{13}CH_3OH$ and one C_3 species derived from 1-$^{12}C_3H_7OH$ (e.g., steps IX and X, XI or step VII). The amounts of unlabeled isobutyraldehyde and isobutanol detected are very similar, and they correspond to those expected from the presence of some ^{12}C in methanol and some ^{13}C in 1-propanol, both of which arise from reverse aldol reactions.

The fragmentation pattern of isobutyraldehyde products shows that the ^{13}C is located predominantly in the CH_3 group (16 amu), with a much smaller but detectable amount in the $CH{=}O$ (29, 30 amu) fragment. The presence of ^{13}C in the aldehydic fragment confirms the formation of some isobutyraldehyde via dehydration of intermediates (step XIX) after isomerization from aldol to keto forms (step XVIII). These pathways involve the retention of the oxygen atom in $^{13}CH_3OH$ within the aldehyde condensation product; they have been shown to occur during the synthesis of branched alcohols from CO and H_2 on Cs–Cu/ZnO (41) and K–$Cu_zMg_5CeO_x$ (8, 21).

The location of the ^{13}C-atom in isobutanol can be measured by comparing the spectra for unlabeled isobutanol (Fig. 9a) with that of the isobutanol formed during reaction (Fig. 9b). Unlabeled isobutanol shows a peak at 31 amu, corresponding to $(CH_2OH)^+$ fragments formed by cleavage of the C–C bond in the β-position to the oxygen atom (42). This peak gives rise to another peak at 33 amu after the transfer of two hydrogen atoms (CH_3–O^+H_2) (42). The peak at 31 amu is less intense than in linear alcohols because the isopropyl fragment formed from isopropanol (43 amu) is branched and leads to a much more stable positively charged fragment. The fragment at 15 amu in the unlabeled isobutanol spectrum corresponds to the methyl group.

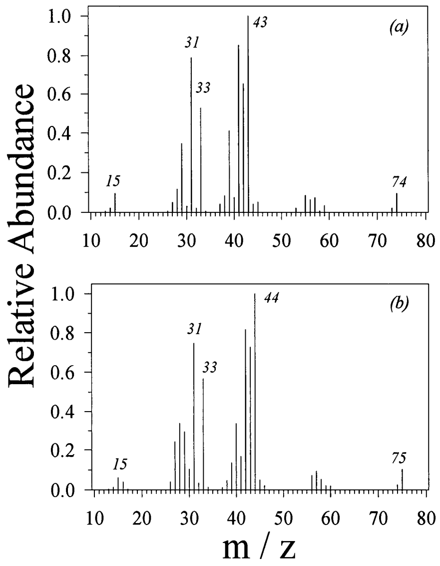

FIG. 9. Mass spectra of (a) unlabeled isobutanol and (b) isobutanol obtained during reaction of $^{13}CH_3OH/1$–$^{12}C_3H_7OH$ mixtures on Mg_1AlO_x [573 K, 101.3 kPa total pressure, 2.7 kPa methanol, 1.4 kPa 1-propanol, balance He, 2.8 h reaction time].

Figure 9b shows the mass spectrum for isobutanol formed from $^{13}CH_3OH/1$–$^{12}C_3H_7OH$ mixtures on Mg_1AlO_x and containing mostly singly labeled molecules. This spectrum contains peaks at 31 and 33 amu, as in the unlabeled spectrum, and very small peaks at 32 and 34 amu, which reflect the presence of ^{13}C in the OH-containing fragments. Isopropyl fragments in the isobutanol products appear at 44 amu, consistent with the presence of a single ^{13}C in this fragment. The spectrum in Fig. 9b also shows that the methyl group of isopropyl fragments contains about 50% of ^{13}C (peak at $m/z = 16$). These results show that the ^{13}C in labeled isobutanol is located in the methyl group of $^{13}CH_3CH(CH_3)$–CH_2OH species. In contrast with the findings for iso-C_4H_8O fragmentation, the amount of $CH_3CH(CH_3){}^{13}CH_2OH$ formed in step XX is negligible (32 or 34 amu peaks in Fig. 9b). The absence of significant amounts of iso-C_4H_9OH labeled at the α-C suggests that cross-coupling reactions of methanol/1-propanol mixtures on Mg_yAlO_x samples occur mainly via a normal Guerbet-type condensation (43, 44) (step VII or IX, X, and XI), and that the contribution of the aldol-keto equilibrium (steps XVIII, XIX, and XX) to iso-C_4H_9OH formation is negligible, probably because of the consecutive nature of step XX.

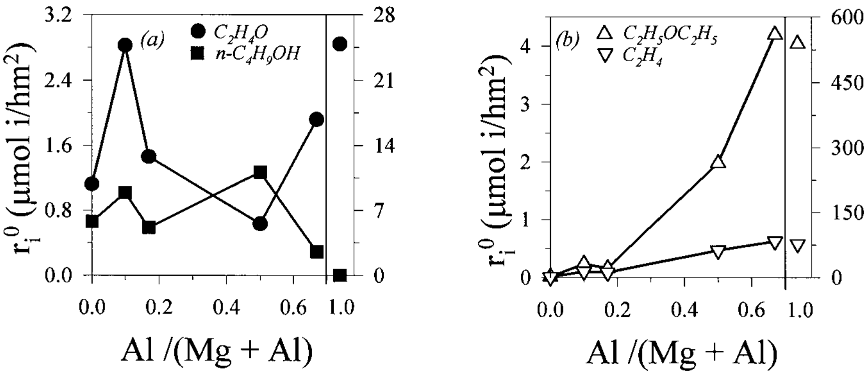

FIG. 10. Product distribution for ethanol conversion reactions on MgO, Al_2O_3, and Mg_yAlO_x samples. Initial formation rates as a function of the sample composition: (a) products of dehydrogenation and condensation reactions, (b) products of dehydration reactions. (573 K, 101.3 kPa total pressure, N_2/ethanol = 10, $X^0_{C_2H_5OH} \cong 5\%$).

5. Sample Composition, Surface Base Property, and Catalytic Performance

C_2H_5OH and CH_3OH/C_3H_7OH mixtures undergo dehydrogenation, dehydration, and condensation reactions on Mg_yAlO_x samples. C_2H_5OH and CH_3OH/C_3H_7OH conversion rates were measured for MgO, Al_2O_3, and Mg_yAlO_x samples at 573 K. Figures 10 and 11 show the product distribution for dehydrogenation and coupling reactions (Figs. 10a and 11a) and for dehydration reactions (Figs. 10b and 11b). A comparison of the data in Figs. 10 and 11 suggests a similar effect of chemical composition on the product distribution from C_2H_5OH and CH_3OH/C_3H_7OH reactants. While MgO and Mg-rich Mg_yAlO_x mixed oxides behave as solid basic catalysts and convert short-chain linear alcohols predominantly into aldehydes or higher alcohols, Al-rich Mg_yAlO_x samples and Al_2O_3 mainly dehydrate alcohols to ethers and to a lesser extent to olefins.

Pure MgO is active for dehydrogenation and coupling reactions but shows negligible dehydration activity. The introduction of small amounts of Al^{3+} ions into the MgO matrix increases both dehydrogenation and condensation rates, but dehydrogenation (to form C_2H_4O or C_3H_6O) becomes the predominant reaction on Mg-rich samples (Figs. 10a and 11a). The required dehydrogenation steps occur much faster than chain growth reactions, which form higher alcohols and other oxygenates. For C_2H_5OH reactions, n-C_4H_9OH is the main coupling product and it forms at the highest rate on Mg_9AlO_x and Mg_1AlO_x (Fig. 10a). Similarly, iso-C_4H_9OH is the predominant condensation product of CH_3OH/C_3H_7OH cross-coupling reactions and shows maximum rates on Mg_9AlO_x and $Mg_{0.5}AlO_x$ (Fig. 11a). Even though dehydration rates to olefins and ethers increase with increasing Al content (Figs. 10b and 11b), none of the samples was very active for olefin synthesis (C_2H_4 or C_3H_6) and ethers were the predominant dehydration products ($C_2H_5OC_2H_5$, Fig. 10b, or CH_3OCH_3, $CH_3OC_3H_7$, and $C_3H_7OC_3H_7$, Fig. 11b). Pure Al_2O_3 is about two orders of magnitude more active than any of the Mg_yAlO_x samples in alcohol dehydration reactions, but it does not form condensation products such as n-C_4H_9OH and iso-C_4H_9OH.

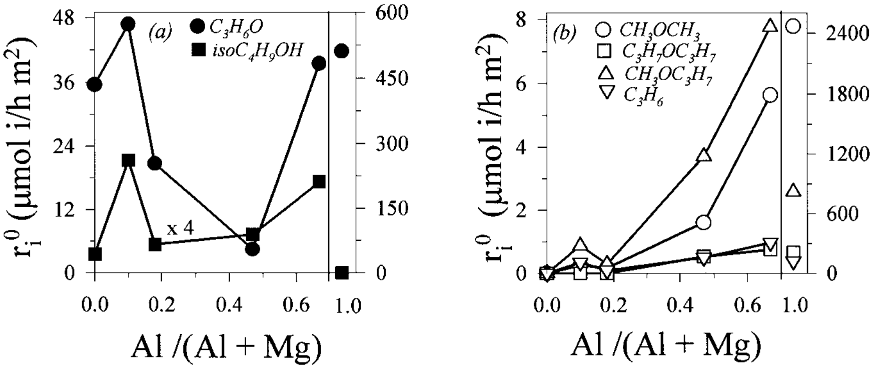

FIG. 11. Product distribution for methanol/1-propanol conversion reactions on MgO, Al_2O_3, and Mg_yAlO_x samples. Initial formation rates as a function of the sample composition: (a) products of dehydrogenation and condensation reactions, (b) products of dehydration reactions. (573 K, 101.3 kPa total pressure, $W = 0.038$ g, 2.7 kPa methanol, 1.4 kPa 1-propanol, balance He.)

In summary, the data shown in Figs. 10 and 11 show that both the total reaction rates and the product selectivity for C_2H_5OH or CH_3OH/C_3H_7OH conversion reactions depend on the chemical composition of the Mg_yAlO_x samples. In turn, the chemical composition affects the acid–base properties of Mg_yAlO_x samples by modifying surface acid and base site densities and the distribution of strength for such sites. The data shown in Table 2 and the infrared spectra of adsorbed CO_2 reported elsewhere (20) show that Mg_yAlO_x catalysts exhibit three types of basic sites, isolated O^{2-}ions, Mg^{2+}–O^{2-} pairs, and OH groups. Pure MgO contains the highest concentration of strongly basic O^{2-}, but as the Al content increases, the relative concentrations of the other weaker basic sites increases; the density of acid sites concurrently increases. Lewis acid sites provided by coordinatively unsaturated Mg^{2+} and Al^{3+} centers bind basic molecules more strongly than Brønsted acid sites provided by OH groups at the surface of Mg_yAlO_x samples (Fig. 1). The results of isotopic switch measurements (Table 2) also show that the contribution from Al^{3+}–O^{2-} pairs to Al_2O_3 surface basicity is not significant. The rest of this paper attempts to bring together into a cogent structure–function relationship the effects of sample composition on surface acid–base properties and on the rates of each major reaction pathway involved in alcohol conversion reactions on Mg_yAlO_x samples.

Dehydration of alcohols to olefins on Mg_yAlO_x samples can proceed through the two elimination mechanisms (E_2 and E_{1cB}) shown in Scheme 1. The E_2 elimination is a single-step concerted mechanism, in which the OH group and the β-H are simultaneously abstracted by a Lewis acid–Brønsted base pair site of balanced strength (like the Al^{3+}–O^{2-} pairs in Al_2O_3). This mechanism leads to the formation of olefins without involving ionic intermediates (45, 46). In contrast, E_{1cB} pathways involve surface alkoxy intermediate and both strongly basic sites and weak Lewis acid sites (e.g., Mg^{2+}–O^{2-} pairs in MgO) (46). Formation of the olefin takes place by β-H elimination from carbanion intermediates.

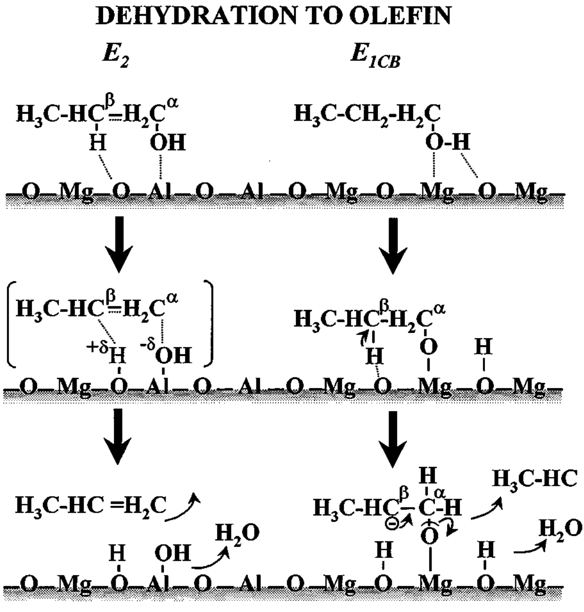

SCHEME 1. Propylene formation mechanisms in methanol/1-propanol conversion reactions.

Pure MgO and Mg-rich samples contain strong basic sites (Table 2) consisting of O^{2-} anions, which catalyze alcohol dehydration to olefins via E_{1cB} pathways. The rate of alcohol dehydration to olefins increases with increasing Al content on Mg_yAlO_x catalysts, because the incorporation of the more electronegative Al^{3+} ions increases the density and strength of acid sites (Table 2) and thus decreases the activation energy for β-H abstraction (47). Aluminum-rich Mg_yAlO_x samples contain a relatively high density of Al^{3+}–O^{2-} pairs, a higher number of acidic sites, and a lower density of basic sites (Table 2). Therefore, alcohol dehydration to C_2H_4 or C_3H_6 on these samples is more likely to proceed through an E_2 elimination mechanism. Pure alumina, a typical E_2 catalyst, is 10^2–10^3 times more active in olefin synthesis from ethanol or 1-propanol than Mg_yAlO_x samples.

Both ethanol and methanol/1-propanol mixtures lead to ether/olefin molar ratios greater than one over the entire range of composition of Mg_yAlO_x samples, and these ratios increase with increasing Al content. Dehydration of primary alcohols to olefins is usually the predominant reaction on strongly acidic oxides, which contain small, highly charged cations (38), whereas ether formation takes place on less acidic oxides (37, 48, 49). Alcohol dehydration to olefins has a higher activation energy than the competitive dehydration to ethers, and it is favored at high reaction temperatures. Mg_yAlO_x samples are weakly acidic (Table 2), and alcohol reactions were studied at relatively low temperatures; both of these contribute to the predominant formation of ethers on the Al_2O_3 and Al-rich Mg_yAlO_x samples of this study.

Ether formation is a second-order reaction that involves the adsorption of two alcohol molecules on neighboring active sites offering different acid–base properties (20, 37). As shown in Scheme 2, one alcohol molecule adsorbs through the oxygen of the OH group on a Lewis acid site, which is also involved in olefin formation via an E_2 mechanism (37). The other alcohol molecule adsorbs on a basic site via the hydroxylic hydrogen and forms an incipient surface alkoxide. On our Mg_yAlO_x samples, the active acid sites for ether formation from primary alcohols are probably the Al^{3+} cations or even the acidic OH groups, as also proposed for zeolites (50), whereas the basic sites are the neighboring O^{2-}ions. The abundance of surface Al^{3+}–O^{2-} pairs accounts for the high ether formation rates observed on Al_2O_3 and Al-rich Mg_yAlO_x samples.

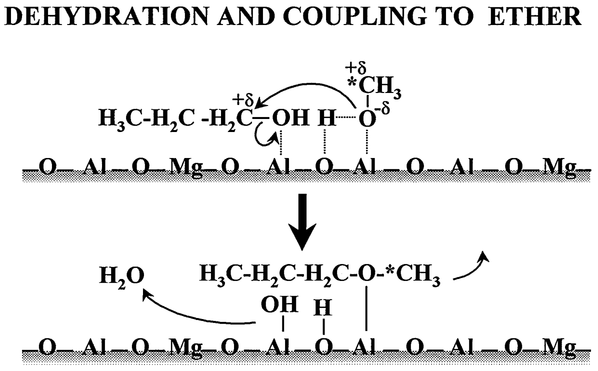

SCHEME 2. Methyl-propyl ether formation mechanism in methanol/1-propanol conversion reactions.

Only the symmetrical ether ($C_2H_5OC_2H_5$) can form from ethanol, whereas three ethers, two symmetrical (CH_3OCH_3 and $C_3H_7OC_3H_7$) and one asymmetrical ($CH_3OC_3H_7$), can form from $CH_3OH + C_3H_7OH$ mixtures. Ether formation involves adjacent adsorption of two alcohol molecules, and reaction rates and selectivities depend sensitively on the molecular structure of the alcohols involved. As the alcohol carbon chain grows, steric factors cause the ether production to decrease (51). This explains the rate formation order $CH_3OCH_3 > C_2H_5OC_2H_5 \gg C_3H_7OC_3H_7$ (Figs. 10b and 11b).

In summary, dehydration reactions to either olefins or ethers on Mg_yAlO_x samples appear to occur on Lewis acid–Brønsted base sites (Mg^{2+}–O^{2-} or Al^{3+}–O^{2-} pairs) or on weakly basic Brønsted sites (OH groups), both of which are abundant in Al-rich samples and on Al_2O_3.

Dehydrogenation of alcohols to aldehydes (C_2H_4O or C_3H_6O) is a typical base-catalyzed reaction (38, 45, 52), the site requirements for which have been disussed previously for ethanol dehydrogenation reactions (20). Mg^{2+}–O^{2-} pairs with moderately basic oxygens play an important role, because weak Lewis acid–strong Brønsted base site pairs are required for hydrogen abstraction steps leading to alkoxy intermediates. As shown in Scheme 3, dehydrogenation starts by alcohol chemisorption on Mg^{2+}–O^{2-} site pairs, which cleave O–H bonds to form surface alkoxide intermediates bound to the Mg^{2+} acid center. The α-hydrogen in the alkoxide group is then abstracted by a neighboring basic site in order to form adsorbed aldehydes. Thus, synthesis of C_2H_4O or C_3H_6O, from ethanol or 1-propanol, respectively, prevails on basic oxides such as Mg-rich Mg_yAlO_x samples with abundant Mg^{2+}–O^{2-} site pairs (Table 2). These samples show Al surface enrichment, and the surface Al species provide additional Lewis centers to stabilize alkoxide intermediates. These results suggest that Al–O–Mg species may be particularly effective and abundant sites for dehydrogenation reactions on Mg-rich samples. In contrast, pure MgO contains a high density of isolated O^{2-} ions, which are strongly basic, but which lack sufficiently strong conjugated Lewis acid pairs to stabilize the alkoxy intermediates. As a result, pure MgO shows lower dehydrogenation rates than Mg-rich Mg_yAlO_x catalysts.

The compositional trends observed for H_2–D_2 equilibration rates (Fig. 3) and alcohol dehydrogenation (Figs. 10a and 11a) on MgO and Mg-rich samples are similar, suggesting that both reactions involve rate-determining steps requiring similar surface sites. In contrast, on Al-rich samples the aldehyde formation rate increases with increasing Al content, while H_2–D_2 equilibration rates remain relatively independent of composition. These results suggest that $H_2(D_2)$ dissociation and O–H or C–H bond activation benefit from the presence of Al–O–Mg sites on Mg-rich Mg_yAlO_x samples, but that on more electronegative Al-rich catalysts only the C–H bond activation can be efficiently performed. Its is probable that Al^{3+}–O^{2-} pairs contribute to aldehyde formation on Al-rich Mg_yAlO_x samples. For instance, it has been reported that on Al_2O_3 activated at low temperatures, alcohol dehydrogenation is largely determined by the density of structural defects, specifically Al vacancies (53). Al-rich Mg_yAlO_x samples contain a high density of Al–O pairs with unsaturated surface aluminum cations, which can form aldehydes via the abstraction of the α-hydrogen as a hydride, as reported for ZnO and Cr_2O_3 (54).

The dependence of dehydrogenation and condensation rates on catalyst composition (Figs. 10a and 11a) are qualitatively similar, suggesting that both reactions require common intermediates and similar acid–base surface properties. Condensation reactions also proceed via a combined mechanism in which the role of Al–O pairs is to increase the rate of formation of alkoxide intermediates and of the primary aldehyde products (Scheme 4). Pure alumina, however, does not form n-butanol or isobutanol, suggesting that

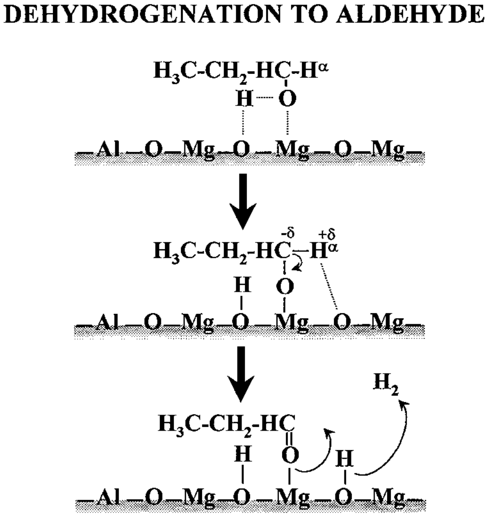

SCHEME 3. Propionaldehyde formation mechanism in methanol/1-propanol conversion reactions.

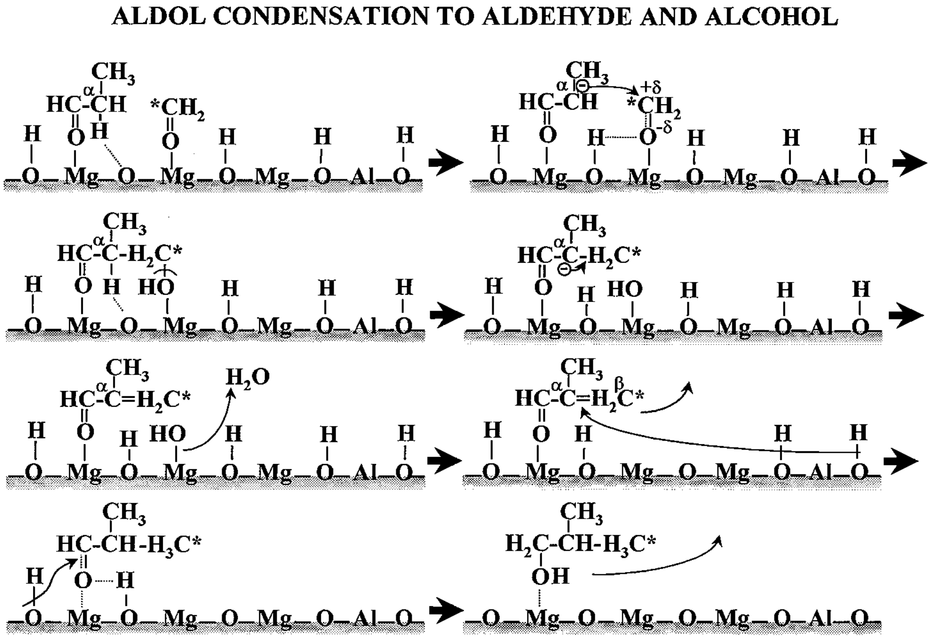

SCHEME 4. Isobutyraldehyde and isobutanol formation mechanism in methanol/1-propanol conversion reactions.

Al–O pairs, which can activate the C–H bond, do not promote the formation of C–C bonds required for aldol condensation reactions.

Reactions leading to n-C_4H_9OH (or n-C_4H_8O) and iso-C_4H_9OH (or iso-C_4H_8O) are much slower than ethanol and 1-propanol dehydrogenation reactions (Figs. 10a and 11a). This reflects the bimolecular nature of condensation reactions, which require not only the proper acid–base pair sites but also a particular surface atom arrangement that can accommodate vicinal adsorbed species. This may also explain why the rate of formation of iso-C_4H_9OH via cross-coupling reactions of CH_3OH and 1-C_3H_7OH (Fig. 11a) is lower than the rate of formation of n-C_4H_9OH in the self-coupling reaction of ethanol (Fig. 10a), because the former requires the adjacent adsorption of C_1 species and bulkier C_3-derived species. Furthermore, substitution of the α-C in the aldehydic intermediates of aldol condensation reactions (C_3H_6O in Scheme 4) defines the stability of the carbanion formed and also explains the higher reactivity toward condensation of C_2H_4O compared to C_3H_6O. Also, as stated previously, formaldehyde was not detected among dehydrogenation products. Noller *et al.* (55) have shown using temperature-programmed reactions of pre-adsorbed methanol that on basic oxides, such as MgO, formaldehyde is decomposed to CO and H_2 immediately upon formation. In contrast, formaldehyde desorbs before decomposition on more acidic oxides. Therefore, on strongly basic oxide surfaces formaldehyde-type intermediates would be present in much lower concentrations, a situation that disfavors the cross-coupling reactions leading to isobutanol and isobutyraldehyde (step IX in Fig. 8).

CONCLUSIONS

The rates and product distributions for C_2H_5OH or CH_3OH/C_3H_7OH reactions are strongly influenced by the composition of Mg_yAlO_x samples prepared by decomposition of hydrotalcite precursors. The rate of alcohol dehydration to ethers and olefins increases markedly with increasing Al content. Al-rich Mg_yAlO_x samples contain a high density of Al^{3+}–O^{2-} site pairs and of moderate-strength basic sites, the combination of which promote the formation of ethylene or propylene from primary alcohols via E_2 elimination pathways. The parallel dehydration pathways to form ethers involve two adjacent alcohol-derived adsorbed species interacting with neighboring acid–base pair sites. On Mg_yAlO_x samples, the acid sites required for ether formation probably consist of Al^{3+} cations, while the basic sites are provided by the corresponding O^{2-} anions. The abundance of surface Al^{3+}–O^{2-} pairs accounts for the high ether formation rates observed on Al_2O_3 and Al-rich Mg_yAlO_x samples.

The dehydrogenation of alcohols to aldehydes (C_2H_4O or C_3H_6O) requires weak Lewis acid–strong Brønsted base site pairs in order to form and stabilize alkoxide intermediates. The synthesis of C_2H_4O or C_3H_6O is favored on Mg-rich Mg_yAlO_x samples because these samples contain a much larger number of properly positioned Al^{3+} Lewis acid sites and Mg^{2+}–O^{2-} basic pairs, which catalyze C–H and O–H activation steps in alcohol dehydrogenation reactions. Mixed Al–O–Mg sites are also active for the mechanistically related heterolytic dissociation of H_2 (and D_2) molecules in H_2–D_2 isotopic equilibration reactions, which are also favored on Mg-rich Mg_yAlO_x samples.

Aldol condensation reactions on Mg_yAlO_x samples involve also the formation of a carbanion intermediate on Lewis acid–strong Brønsted base pair sites, and consequently they are also favored on Mg-rich samples. The formation rates of n-C_4H_8O and n-C_4H_9OH or iso-C_4H_9OH and iso-C_4H_8O are slower than dehydrogenation reactions because in bimolecular aldol condensations not only the acid–base surface properties are relevant but also the surface atom arrangement needed to adsorb adjacent species and the steric factors related to the chemical nature of the parent alcohols and aldehydic intermediates.

ACKNOWLEDGMENTS

This work was supported by the U.S. Department of Energy, the National Science Foundation (U.S.A.), and CONICET (Argentina). The authors thank Dr. M. Xu for his technical assistance with the CO_2 isotopic switch experiments. M. J. L. Gines acknowledges the Universidad Nacional del Litoral, Santa Fe, Argentina, for a fellowship for post-doctoral studies at the University of California at Berkeley.

REFERENCES

1. Schneider, M., Kochloefl, K., and Bock, O., Eur. Patent Appl. 152, 809, 1985.
2. Sugier, A., and Freund, E., U.S. Patent 4,112,110, 1978.
3. Di Cosimo, J. I., Marchi, A. J., and Apesteguía, C. R., *J. Catal.* **134**, 594 (1992).
4. Nunan, J. G., Bogdan, C. E., Klier, K., Smith, K. J., Young, C., and Herman, R. G., *J. Catal.* **116**, 195 (1989).
5. Forzatti, P., Tronconi, E., and Pasquon, I., *Catal. Rev. Sci. Eng.* **33**, 109 (1991).
6. Apesteguía, C. R., Soled, S. L., and Miseo, S., U.S. Patent 5,387,570, 1995.
7. Apesteguia, C. R., De Rites, B., Miseo, S., and Soled, S. L., *Catal. Lett.* **44**, 1 (1997).
8. Xu, M., Ginés, M. J. L., Hilmen, A., Stephens, B. L., and Iglesia, E., *J. Catal.* **171**, 130 (1997).
9. Xu, M., and Iglesia, E., *Catal. Lett.* **51**, 47 (1998).
10. Bowker, M., Hadden, R. A., Houghton, H., Hyland, J. N. K., and Waugh, K. C., *J. Catal.* **109**, 263 (1988).
11. Neophytides, S. G., Marchi, A. J., and Froment, G. F., *Appl. Catal. A* **86**, 45 (1992).
12. Reichle, W. T., *J. Catal.* **94**, 547 (1985).
13. Rao, K. K., Gravelle, M., Sanchez Valente, J., and Figueras, F., *J. Catal.* **173**, 115 (1998).
14. Di Cosimo, J. I., Diez, V. K., and Apesteguía, C. R., *Appl. Clay Sci.* **13**, 433 (1998).
15. Velu, S., and Swamy, C. S., *Appl. Catal.* **119**, 241 (1994).
16. Corma, A., Iborra, S., Primo, J., and Rey, F., *Appl. Catal.* **114**, 215 (1994).
17. Kumbhar, P., Sanchez Valente, J., and Figueras, F., *J. Chem. Soc. Chem. Commun.*, 1091 (1998).
18. Schaper, H., Berg-Slot, J. J., and Stork, W. H. J., *Appl. Catal.* **54**, 79 (1989).
19. Corma, A., Fornés, V., and Rey, F., *J. Catal.* **148**, 205 (1994).
20. Di Cosimo, J. I., Diez, V. K., Xu, M., Iglesia, E., and Apesteguia, C. R., *J. Catal.* **178**, 499 (1998).
21. Ginés, M. J. L., and Iglesia, E., *J. Catal.* **176**, 155 (1998).
22. Price, G. L., and Iglesia, E., *Ind. Eng. Chem.* **28**, 839 (1989).
23. Reichle, W. T., Kang, S. Y., and Everhardt, D. S., *J. Catal.* **101**, 352 (1986).
24. Nakatsuka, T., Kawasaki, H., Yamashita, S., and Kohjiya, S., *Bull. Chem. Soc. Jpn.* **52**, 2449 (1979).
25. Mc Kenzie, A. L., Fishel, C. T., and Davis, R. J., *J. Catal.* **138**, 547 (1992).
26. Shen, J., Tu, M., and Hu, C., *J. Solid State Chem.* **137**, 295 (1998).
27. Eley, D. D., and Zammit, M. A., *J. Catal.* **21**, 366 (1971).
28. Eley, D. D., and Zammit, M. A., *J. Catal.* **21**, 377 (1971).
29. Tsuchiya, S., *J. Catal.* **20**, 1 (1971).
30. Chelseske, F. J., Wallace, W. E., and Hall, W. K., *J. Phys. Chem.* **63**, 505 (1963).
31. Steele, L. R., and Copper, W. H., *J. Catal.* **6**, 147 (1966).
32. Lunsford, J. H., *J. Phys. Chem.* **66**, 2591 (1962).
33. Boudart, M., Delbouille, A., Derouane, E. G., Indovina, V., and Walters, A. B., *J. Am. Chem Soc.* **94**, 6622 (1972).
34. Hattori, H., Tanaka, Y., and Tanabe, K., *J. Am. Chem Soc.* **98**, 4652 (1976).
35. Nakano, Y., Yamaguchi, T., and Tanabe, K., *J. Catal.* **80**, 307 (1983).
36. Kazansky, V. B., Borovkov, V. Y., and Kustov, L. M., *in* "Proceedings 8th International Congress on Catalysis, Berlin, 1984," III-3. Dechema, Frankfurt-am-Main, 1984.
37. Jain, J. R., and Pillai, C. N., *J. Catal.* **9**, 322 (1967).
38. Kibby, C. L., and Hall, W. K., *J. Catal.* **29**, 144 (1973).
39. Takezawa, N., Hanamaki, C., and Kobayashi, H., *J. Catal.* **38**, 101 (1975).
40. Smith, K. J., and Anderson, R. B., *Can. J. Chem. Eng.* **61**, 40 (1983).
41. Nunan, J. G., Bogdan, C. E., Herman, R. G., and Klier, K., *Catal. Lett.* **2**, 49 (1989).
42. Beynon, J. H., Saunders, R. A., and Williams, A. E., *in* "The Mass Spectra of Organic Molecules." Elsevier, New York, 1968.
43. Ueda, W., Ohshida, T., Kuwabara, T., and Morikawa, Y., *Catal. Lett.* **12**, 97 (1992).
44. Ueda, W., Ohowa, H., Iwasaki, K., Kubawara, T., Ohshida, T., and Morikawa, Y., *in* "Acid–Base Catalysis II." Kodansha-Elsevier, Tokyo, 1994.
45. Tanabe, K., Misono, M., Ono, Y., and Hatori, H., *in* "New Solid Acid and Bases." Kodansha-Elsevier, Tokyo, 1989.
46. Gervasini, A., Fenyvesi, J., and Auroux, A., *Catal. Lett.* **43**, 219 (1997).
47. Parrott, S. L., Rogers, J. W., and White, J. M., *Appl. Surf. Sci.* **1**, 443 (1978).
48. Padmanabhan, V. R., and Eastburn, F. J., *J. Catal.* **24**, 88 (1972).
49. Luy, J. C., and Parera, J. M., *Appl. Catal.* **26**, 295 (1986).
50. Jacobs, P. A., Tielen, M., and Uytterhoeven, J. B., *J. Catal.* **50**, 98 (1977).
51. Simonik, J., and Pines, H., *J. Catal.* **24**, 211 (1972).
52. Canesson, P., and Blanchard, M., *J. Catal.* **42**, 205 (1979).
53. Wang, J. A., Bokhimi, X., Novaro, O., Lopez, T., Tzompantzi, F., Gomez, R., Navarrete, J., Llanos, M. E., and Lopez-Salinas, E., *J. Molec. Catal.* **137**, 239 (1999).
54. Burwell, R. L., *Catal. Rev.* **7**, 25 (1972).
55. Noller, H., and Ritter, G., *J. Chem. Soc. Faraday Trans. I* **80**, 275 (1984).